IOP Publishing Journal of Physics D: Applied Physics
J. Phys. D: Appl. Phys. **53** (2020) 375103 (7pp) https://doi.org/10.1088/1361-6463/ab938b

Factors limiting carrier transport of ultrathin W-doped In_2O_3 films

Yutaka Furubayashi[1], **Makoto Maehara**[2] **and Tetsuya Yamamoto**[1]

[1] Materials Design Center, Research Institute, Kochi University of Technology, Tosayamadacho-Miyanokuchi 185, Kami 782-8502 Japan
[2] Industrial Equipment Division, Sumitomo Heavy Industries, Ltd., Soubiraki-cho 5-2, Niihama 792-8588 Japan

E-mail: furubayashi.yutaka@kochi-tech.ac.jp

Received 26 March 2020, revised 3 May 2020
Accepted for publication 15 May 2020
Published 29 June 2020

Abstract

Polycrystalline ultrathin 5 nm-thick *n*-type W-doped In_2O_3 (*p*-IWO) films with a significantly high Hall mobility (μ_H) of 57.7 cm^2 $(Vs)^{-1}$ were successfully fabricated by the under-vacuum solid-state crystallization of amorphous IWO (*a*-IWO) films. *a*-IWO films with thicknesses (*t*) ranging from 5 to 50 nm were deposited on glass substrates without intentionally heating the substrates by reactive plasma deposition with direct current arc discharge. The source used for the film growth was a sintered In_2O_3 pellet with a WO_3 content of 1.0 wt.% (corresponding to 0.6 at.%). We investigated the *t* dependence of the carrier transport mechanism of IWO films having the mean free paths of carrier electrons similar to *t* based on an empirical model with combined surface and interface scattering. The qualitative analysis of the relationship between μ_H and the ratio of the mean free path of carriers in the bulk material of *n*-type to *t* proved that the contribution of the combined scattering to μ_H is significantly dominant for *p*-IWO films at *t* of less than 10 nm. In such films that have very smooth surface with roughness of less than 0.78 nm and interface with roughness of less than 1 nm, the combined specularity parameter (≤ 2) is found to be 1.6 to 1.7, resulting in a high μ_H.

Keywords: indium oxides, ultra thin film, high Hall mobility, classical-size-effect model

(Some figures may appear in colour only in the online journal)

1. Introduction

Indium oxide (In_2O_3) has a cubic bixbyite crystal structure (space group *Ia*-3, number 206) [1, 2]. High-level *n*-type doped In_2O_3 films have been mostly used as transparent conducting oxide (TCO) films [3–5] and applied in thin-film transistors [6, 7]. Although Sn-doped In_2O_3 (ITO) films have been conventionally adopted as TCO films, a higher Hall mobility (μ_H) will be required for wide applications. The advantages of alternative dopants such as hydrogen [8], cerium [9, 10], and tungsten (W) [10–14] over Sn donors have recently been investigated to achieve In_2O_3-based TCO films showing a high μ_H for use as a top electrode of solar cells.

Note that the carrier transport properties of films strongly depend on film thickness (*t*). For thick TCO films showing a high μ_H, with decreasing *t* down to 20 nm, we found a decrease in μ_H owing to the discontinuity or surface roughness of the films [6, 15, 16]. In our previous work [17], we successfully fabricated ultrathin amorphous ITO (*a*-ITO) films showing a high μ_H of more than 40 cm^2 $(Vs)^{-1}$ with *t* of less than 10 nm. The *a*-ITO films were deposited on glass substrates by reactive plasma deposition with direct current arc plasma (RPD) [14, 17–20]. We analyzed the transport properties of *a*-ITO films in terms of the bulk density of *a*-ITO films and the ratio of *t* to the mean free path of free carriers (λ_{MFP}) on the basis of a classical-size effect model [17].

In this article, we demonstrated that a solid-state crystallization process in a vacuum environment inducing transformation from amorphous to polycrystalline W-doped In_2O_3 (*p*-IWO) films produced high-μ_H films. Amorphous IWO (*a*-IWO) films were deposited on glass substrates by RPD. The reasons we chose W atoms as a better alternative to Sn donors are as follows. First, the valence *s* orbitals of W atoms with antibonding states will be largely extended spatially,

compared with those of Sn atoms. The energy level of valence *s* orbitals with respect to the vacuum level of W (6.20 eV) is smaller than that of Sn (12.50 eV) [21]. The valence *s* electrons of W atoms should largely contribute to the antibonding states, i.e. the conduction band generated by the strong hybridization between W 6*s*, In 5*s* and O 2*p* orbitals. In addition, the radius of the valence *s* orbitals of W atoms (0.165 nm) is larger than that of Sn (0.114 nm) atoms [22]. These effects would promote a high μ_H. The second reason is that W atoms have a high affinity for O atoms: the dissociation energy for the W–O bond of 720 kJ mol^{-1} is higher than that for the Sn–O bond (528 kJ mol^{-1}) [23]. This high affinity between O and W atoms suppresses the formation of O vacancies (V_O) and consequently enhances edge sharing [17] of In(W)–O or W atom on In site networks. The edge-sharing structure allows a large overlap of the antibonding wavefunctions of the valence *s* electrons between In and W atoms, which will also produce a high μ_H [5, 14, 24]. We will clarify the specific and unique effects of W doping on the electrical properties by comparing the Hall effect measurement results between ITO and IWO films. Note that for ultrathin films, the study on the contribution of the surface and interface scattering on the carrier transport is essential considering the use of glass substrates. We elucidated the key factors characterizing the carrier transport of IWO films.

2. Experimental

We carried out under-vacuum solid-state crystallization to transform *a*-IWO films to *p*-IWO films [9, 10, 14]. *a*-IWO films with *t* ranging from 5 to 50 nm were deposited on non-alkali glass substrates (Corning Eagle XG) by RPD [14, 17–20] without intentionally heating the substrate. The source material used was a sintered In_2O_3 pellet with a WO_3 content of 1.0 wt.% (corresponding to 0.6 at.%), which was pressed into a cylindrical form (height, 40 mm; diameter, 30 mm) and sintered. The flow rates of argon (Ar) gas introduced into the deposition chamber and a plasma gun were 25 and 40 sccm, respectively. The oxygen (O_2) gas flow rate (GFR) for the film growth was 25 sccm. The total pressure during the growth was 0.3 Pa. The typical growth rate was 3.6 nm s^{-1}. After *a*-IWO films were grown, they were subjected to under-vacuum solid-state crystallization in the RPD chamber at a pressure of 5×10^{-4} Pa without any additional gas for 30 min at 250 °C.

X-ray diffraction (XRD) and x-ray reflectivity (XRR) measurements were performed using Rigaku SmartLab with an x-ray source of Cu-Kα1 (wavelength, 0.15405 nm) to determine the structural properties of the *a*-IWO films. The mass density of the film (d_m), the roughnesses of the film surface (r_{sur}) and the interface between the film and the glass substrate (r_{if}), and *t* were determined using the data from the XRR measurements. The electrical properties of the films were determined by Hall effect measurements combined with the van der Pauw geometry (Nanometrics HL5500PC) at room temperature. Optical transmittance and reflectivity were determined using conventional ultraviolet-visible-infrared spectrometer (Hitachi U-4100).

3. Results and discussion

3.1. Crystal structure, mass density and roughness

XRD measurement results showed no crystalline diffraction peaks observed for as-deposited *a*-IWO films regardless of *t* with different plasma-exposure time during film growth, which is not shown in this paper. Figure 1 shows out-of-plane XRD $2\theta/\omega$ patterns for *p*-IWO films with different *t*. In figure 1, we added the data of the mean size (*D*) of crystallites perpendicular to substrate surfaces of all the samples, which was calculated from full widths of half maximum of (222) diffraction peaks using a simple Scherrer formula [25] after subtracting the geometrical smearing [26]. The IWO films prepared by the postannealing process showed cubic structure with a diffraction peak at $2\theta = 30.52°$, corresponding to (222). It can be seen that *p*-IWO films with *t* of more than 19.5 nm except for 50-nm-thick *p*-IWO films showing a (222) orientation mixed with the other orientations have strong (222) preferential orientation, whereas we also found the above peak even for much thinner *p*-IWO films. After the postannealing treatment, there is no evidence of W, WO_3 and WO_{3-x} phases in all the *p*-IWO films. Analysis of the XRD measurement results shows that the lattice constants tend to increase slightly from 1.0095 nm at *t* of 5 nm to 1.0114 nm at *t* of 50 nm, which were almost identical to 1.0118 nm of bulk In_2O_3 and larger than post-annealed IWO films at *t* of 80 nm grown by RPD [14]. Concerning the *t* dependence of *D*, we found the interesting following. For *p*-IWO films with *t* of less than 30 nm, it appears that the upper limit of *D* was limited by *t* during the postannealing process in this work. As a result, residual *D* is almost equal to *t* for the films at any given *t*. On the other hand, at a large *t* of 50 nm, *D* stayed at approximately 60% of *t*. In the case of the thick *p*-IWO films, a texture with a (222) orientation mixed with the other orientations may be associated with the mechanism of complex solid-phase crystallization.

Figure 2 plots the d_m, r_{sur}, and r_{if} of *a*- and *p*-IWO films which were determined by XRR measurements as functions of *t*. The XRR profiles were successfully fitted on the basis of a simple model comprising IWO films and glass substrates without depth-dependent d_m or intermediate layers. This implied the absence of interfacial oxide layers between IWO films and glass substrates. We found insignificant differences in d_m and r_{if} between *a*- and *p*-IWO films at any given *t*. These findings indicate that the solid-state crystallization process caused no evaporation of W and In from the films or no metal segregation at the interface regardless of *t*. On the other hand, in our previous study [17], we found that d_m values of *a*-ITO show a sharp fall down to almost 6.6 g cm^{-3} at *t* of less than 10 nm. The higher d_m of the ultra thin IWO films indicates enhanced atomic packing density as well as decreased numbers of point or structural defects in the films. Such superiority of IWO films to ITO films should be due to high affinity to O atoms of W dopants. The rocking curves for *p*-IWO films at $2\theta = 0.65$ deg showed only a strong specular reflection peak determined by XRR measurements (not shown in the figure). This indicates that the surfaces of *p*-IWO films are flat with excellent spatial uniformity. On the other hand, we found a

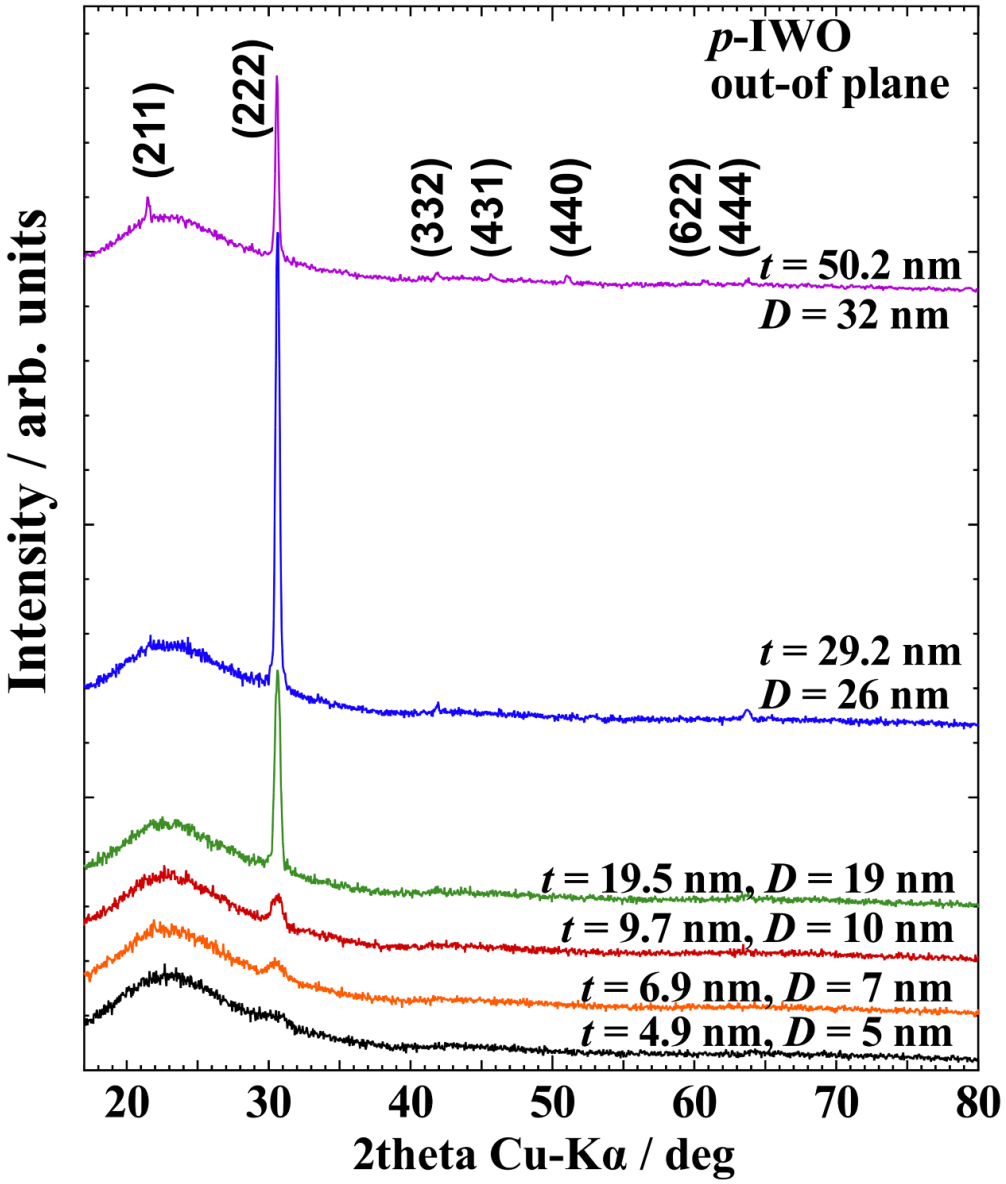

Figure 1. Out-of-plane XRD $2\theta/\omega$ profiles for *p*-IWO films with different thicknesses. Longitudinal grain sizes D for the films derived from (222) diffraction peak are also shown.

reduction in r_{sur} by 0.1 to 0.2 nm for the postannealed *p*-IWO films compared with the as-deposited *a*-IWO films. This may be due to the evolution of a close-packed (222) preferential orientation; the (222) plane is almost parallel to the substrate surface.

3.2. Electrical properties

Figure 3 shows the room-temperature electrical properties of *a*- and *p*-IWO films, namely, electrical resistivity (ρ), carrier concentration (n_e), and μ_H, as functions of t. After the under-vacuum solid-state crystallization process, we found a decrease in the ρ of *p*-IWO films with t of less than 10 nm; in particular, a marked decrease in the ρ of ultrathin 5-nm-thick *p*-IWO films was observed owing to an increase in n_e by threefold. Note that such films showed μ_H of 57.7 cm^2 $(Vs)^{-1}$. On the other hand, n_e decreased and μ_H markedly increased for thicker *p*-IWO films prepared by the solid-state crystallization process. Note that with t of more than 20 nm up to 50 nm, *p*-IWO films showed an increase in μ_H by almost twofold, reaching approximately 97.4 cm^2 $(Vs)^{-1}$. The change in n_e caused by postannealing could be explained as follows. For thick IWO films, a high O affinity of W atoms should produce neutral O interstitials ($O_i^{\times}$) in the neighborhood of W_{In} sites. These notations above are based on the Kröger–Vink notation [27]. The postannealing process produces mobile O_i species, resulting in the following reaction: $O_i^{\times} + V_O^{\bullet} + e' \rightarrow O_O$, where $V_O^{\bullet}$ is an oxygen vacancy with a single positive charge and e' is a free carrier. The annihilation of a single donor $V_O^{\bullet}$ reduces n_e. On the other hand, for thinner IWO films, because of a larger surface area relative to the volume of these films, the removal of O_O from a surface during solid-state

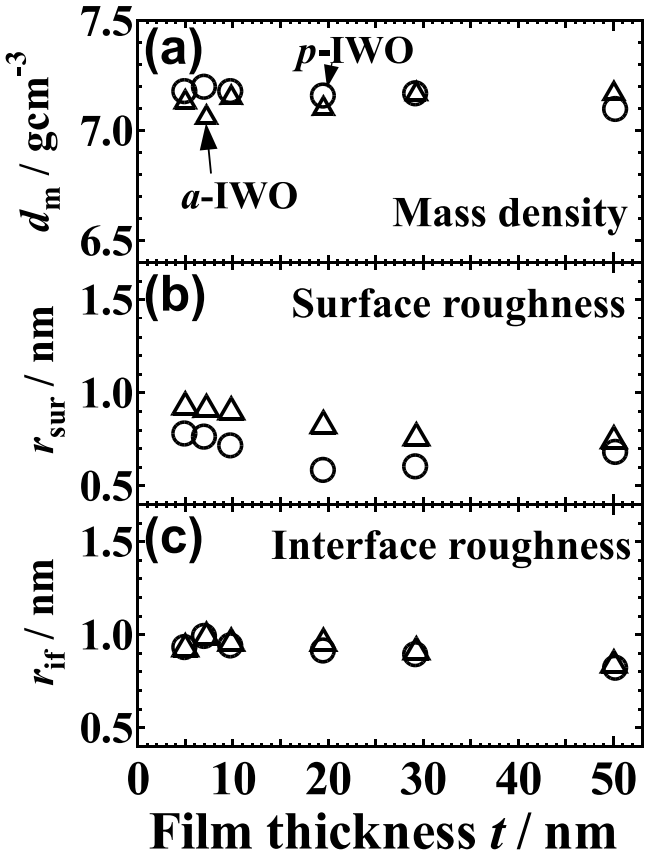

Figure 2. (a) Mass density (d_m), (b) surface roughness (r_{sur}), and (c) interface roughness (r_{if}) of *a*-IWO (triangles) and *p*-IWO films (circles) as functions of thickness (t).

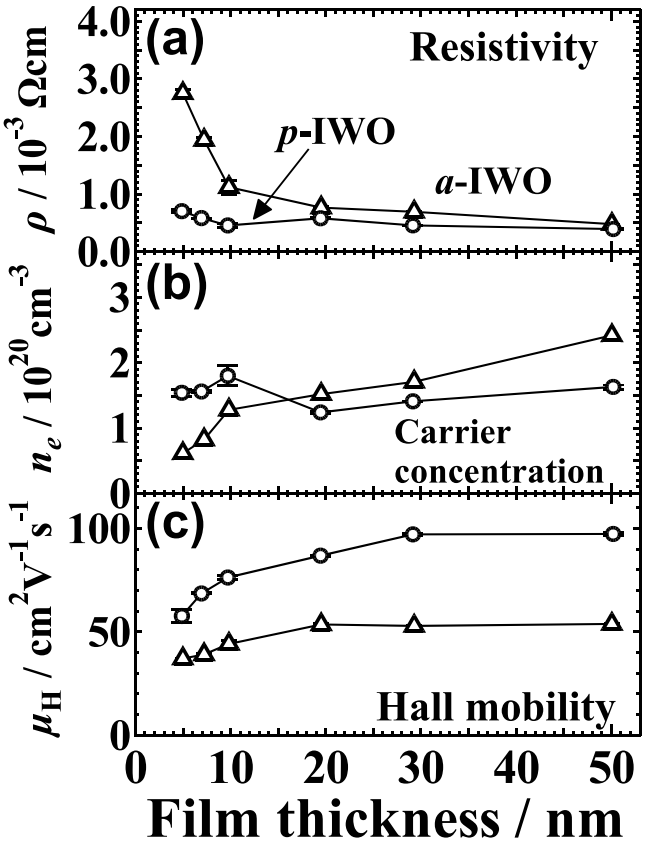

Figure 3. Room-temperature electrical properties of *a*-IWO (triangles) and *p*-IWO films (circles): (a) electrical resistivity (ρ), (b) carrier concentration (n_e), and (c) Hall mobility (μ_H) as functions of film thickness (t).

crystallization increases the density of $V_O^{\bullet}$, resulting in an increase in n_e.

To clarify the features of W doping of In_2O_3 films, ρ, n_e, and μ_H of *a*-ITO films grown at an OFR of 20 sccm [17] and corresponding polycrystalline ITO (*p*-ITO) films in addition to those of *a*- and *p*-IWO films are plotted as functions of t in figure 4. The postannealing condition for obtaining the *p*-ITO films were the same as those for the *p*-IWO films. For ITO films, the postannealing treatment in vacuum increased n_e significantly, resulting in the reduction in μ_H, at any given t. Taking into account the difference in the dissociation energy between Sn-O and W-O bonds, as described in the section 1, this finding leads to a conclusion that the increase of n_e would be originated in an increase in the number of $V_O^{\bullet}$ caused by the above-mentioned treatment for the *a*-ITO films with more unstable O atoms. The further production of $V_O^{\bullet}$ donors enhances the contribution of impurity scattering mechanism to carrier transport; as a consequence of this, μ_H is substantially suppressed as shown in figure 4(c).

Note that d_m of IWO films is almost close to that of bulk In_2O_3 irrespective to t. This makes it possible to investigate the key factors that determine the carrier transport of ultrathin IWO films on the basis of a classical size effect model, as discussed below.

3.3. Classical size effect model

To study the nature of the carrier transport of very thin *a*- and *p*-IWO films with t of less than 30 nm, we take our standpoint that is based on the Ioffe and Regal statement that the mean free path of free carriers (λ_{MFP}) in a metallic system cannot be lower than the electron wavelength: $k_F\lambda_{MFP} > 1$ (where k_F is the magnitude of the wave vector at the Fermi surface) [28]. Note that $k_F\lambda_{MFP}$ is an important physical quantity which characterizes the degree of disorder in a conductor. Assuming a very small contribution of grain boundary scattering to carrier transport and the validity of the Fermi gas model for all the heavily W-doped In_2O_3 films, we thereby calculated the values of relevant electronic parameters, λ_{MFP} [17] and k_F ($=(3\pi^2 n_e)^{1/3}$), using the following expression based on the Fermi gas model:

$$\lambda_{MFP} = \frac{\mu h}{2e}\left(\frac{3n_e}{\pi}\right)^{1/3}, \quad (1)$$

where μ, h, and e denote the mobility of carriers, the Planck constant, and the elemental charge, respectively. Here, we take μ_H as μ. Figures 5(a) and (b) show the λ_{MFP} and $k_F\lambda_{MFP}$ of *a*- and *p*-IWO films as functions of t, respectively. Since λ_{MFP}

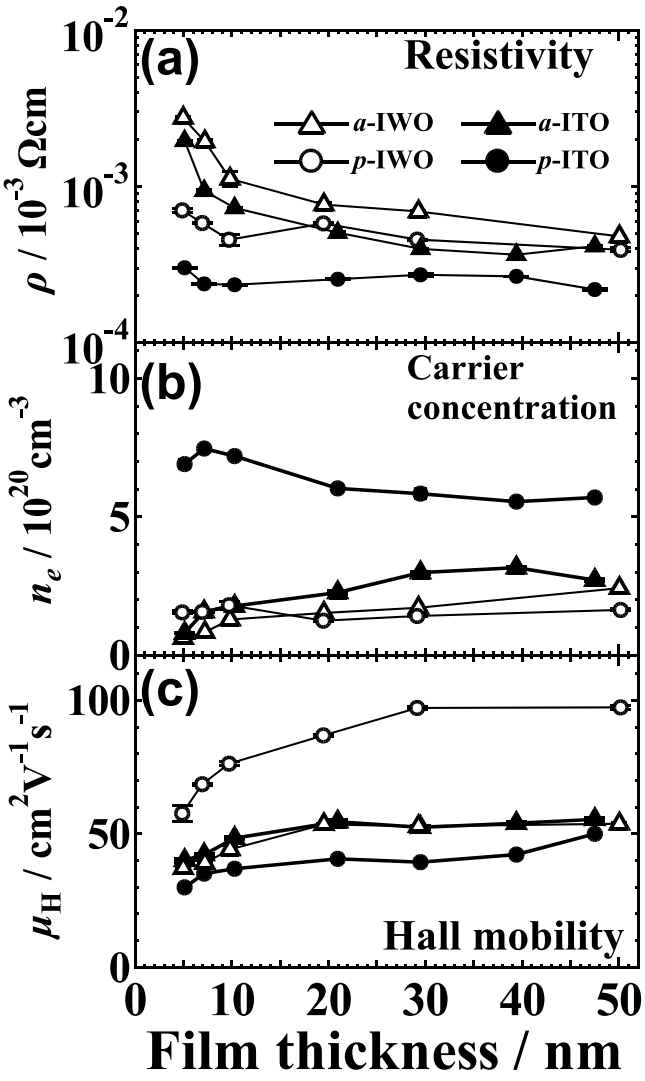

Figure 4. Room-temperature electrical properties of *a*-IWO (triangles) and *p*-IWO films (circles): (a) electrical resistivity (ρ), (b) carrier concentration (n_e), and (c) Hall mobility (μ_H) as functions of film thickness (t). As a comparison, those of *a*-ITO grown at an OFR of 20 sccm (closed triangles) from 17 and corresponding postannealed *p*-ITO films (closed circles) are also shown.

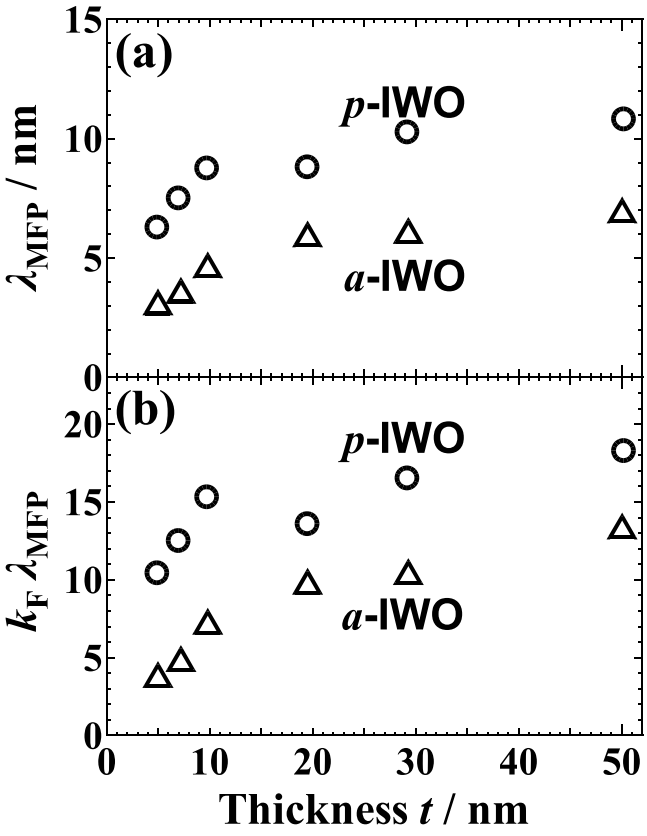

Figure 5. (a) Mean free path of carriers (λ_{MFP}) and (b) product of Fermi wave vector and mean free path ($k_F\lambda_{MFP}$) of *a*-IWO (triangles) and *p*-IWO films (circles) as function of thickness (t).

is proportional to both μ_H and ${n_e}^{1/3}$, as shown by equation (1), the t dependence of λ_{MFP} is similar to that of the μ_H of *a*- and *p*-IWO films. This shows that λ_{MFP} of the *a*- and *p*-IWO films at any given t is larger than the Bohr radius of approximately 2.2 nm of In_2O_3 [29, 30]. We found that t is larger than λ_{MFP} for *a*-IWO films at any given t. On the other hand, note that t is smaller than λ_{MFP} for *p*-IWO films with t of less than 10 nm, whereas t is larger than λ_{MFP} for thicker *p*-IWO films. For all the *p*-IWO films, n_e is of more than 1.2×10^{19} cm^{-3}, as shown in figure 3, and the average distance between carriers (r_s), roughly estimated by $(n_e)^{1/3}$, is of less than 4.4 nm; the minimum value of r_s is twice of the Bohr radius. This would imply a sufficient overlap between the wavefunctions of the electrons in films. Figure 5(b) shows that the condition for the metallic regime: $k_F\lambda_{MFP} > 1$ is satisfied for all the *a*- and *p*-IWO films, in which the transport of charge carriers takes place via de-localized states. For 50-nm-thick *p*-IWO film showing a high $k_F\lambda_{MFP}$ of 18.3, it appears that the random orientation of crystallites shown in figure 1 affected the carrier transport little. Note that figure 5(b) clearly shows a decrease in the disorder parameter $k_F\lambda_{MFP}$ with decreasing t from 10 nm. The t-dependence behavior indicates that the three *p*-IWO with t of less than 10 nm became a weakly disordered metal. Taking into account the fact of little difference in both d_m and r_{if} among *p*-IWO films with different t, as shown in figures 2(a) and (c), that would be due to a t variation in the degree of disorder of $V_O^{\bullet}$ defects near the film surface. From those findings, for *p*-IWO films with t of less than 10 nm, the conductivity that can be treated within the context of the Boltzmann theory should be modified. Considering that figure 3(c) for the very thin films shows that the t dependence of μ_H illustrated typically the classical size effect [31], the electronic processes of the surface or interface states due to the non-uniformity of the spatial distribution of the $V_O^{\bullet}$ defects would affect the properties of the electron scattering, which will be discussed below.

We applied a classical-size-effect model to the three *p*-IWO films with t of less than 10 nm to elucidate key factors that determine carrier transport. In the IWO films, we can distinguish three mechanisms of free-electron scattering: bulk, surface, and interface ones. Each of these scattering mech-

anism has its characteristic relaxation time, and the resultant relaxation time τ_f is given as

$$\tau_f^{-1} = \tau_B^{-1} + \tau_{sur}^{-1} + \tau_{if}^{-1}, \quad (2)$$

where τ_B, τ_{sur}, and τ_{if} denote the relaxation times in the bulk, at the surface and interface scattering, respectively. For the electron mobility in thin films (μ_f), we may use an expression analogous to that for the bulk, i.e. $\mu_f = e\tau_f/m$, where e is the electronic charge and m is the effective mass of the carriers. If all the electrons are not scattered diffusely but a fraction, i.e. p and q, of them are reflected by specular scattering at the surface and interface, respectively, the use of the equation $\mu_f = e\tau_f/m$ should modify the above equation (2) under the assumption that the change in the m of the samples is negligible compared with the variation in carrier mobility to

$$\mu_f = \mu_B/(1 + (2 - (p + q))/\gamma_B), \quad (3)$$

where γ_B is the ratio of the mean free path of the electrons in the bulk material to t. The mobility in a bulk, μ_B, is determined by $\mu_B = e\tau_B/m$. The specularly scattered ($p = q = 1$; $p + q = 2$) electrons do not contribute to the ρ increase, whereas the diffusely scattered electrons with the probability $(1 - p)$ and $(1 - q)$ cause an increase in ρ for very thin p-IWO films. In this study, concerning a μ_B value, we took a large μ_H value of 97.4 cm^2 (Vs)$^{-1}$ of 50 nm thick p-IWO films with n_e of 1.63×10^{20} cm^{-3} and $k_F\lambda_{MFP}$ of 18.3. Using equation (3) and the experimental data of μ_H as μ_f values of the IWO films, we found that the corresponding $(p + q)$ values of very thin p-IWO films varied about 1.6 to 1.7. This finding proved that the specular scattering is still dominant for ultra thin p-IWO films. It could be due to small magnitudes of the r_{sur} and r_{if}, especially, r_{sur} of less than 0.8 nm, as shown in figure 2(b). These findings demonstrate that low r_{sur} and r_{if}, and d_m that is close to that of the bulk film are essential for achieving very thin heavily n-type doped IWO films showing high μ_H.

4. Conclusions

We successfully achieved p-IWO films with a high μ_H prepared by the under-vacuum solid-state crystallization method using a-IWO films deposited on glass substrates by RPD. 5-nm-ultrathin and 50-nm-thick p-IWO films showed (n_e, μ_H) values of (1.54×10^{20} cm^{-3}, 57.7 cm^2 (Vs)$^{-1}$) and (1.63×10^{20} cm^{-3}, 97.4 cm^2 (Vs)$^{-1}$), respectively. For p-IWO films, the experimental result that d_m values remain almost constant at any given t, which is a feature of W doping compared to Sn doping, allows us to investigate the key factors limiting the carrier transport of the IWO films on the basis of a classical size effect model. Quantitative analysis indicated that the size effect becomes dominant for p-IWO films at t of less than 10 nm. In such films that have r_{sur} and r_{if} smaller than 1 nm, the contribution of the combined surface and interface scattering to the μ_H is significantly greater than that of ionized impurity scattering.

Acknowledgments

The authors are grateful to Dr. Nobuaki Takahashi, Mr. Toshiyuki Sakemi, and Mr. Hisashi Kitami of Sumitomo Heavy Industries, Ltd., for helpful discussions during this study. This study was carried out in collaboration with Sumitomo Heavy Industries, Ltd. (Patent: WO2017/014278A1 (Sumitomo Heavy Industries, Ltd.), 2017-01-26).

ORCID iDs

Yutaka Furubayashi https://orcid.org/0000-0001-8136-2553
Tetsuya Yamamoto https://orcid.org/0000-0002-7317-1252

References

[1] Buchholz D B, Ma Q, Alducin D, Ponce A, Jose-Yacaman M, Khanal R, Medvedeva J E and Chang R P H 2014 *Chem. Mater.* **26** 5401
[2] González G B, Mason T O and Quintana J P 2004 *J. Appl. Phys.* **96** 3912
[3] Ginley D S and Bright C 2000 *MRS Bull.* **25** 15
[4] Hamberg I and Granqvist C G 1986 *J. Appl. Phys.* **60** R123
[5] Calnan S and Tiwari A N 2010 *Thin Solid Films* **518** 1839
[6] Miyasako T, Senoo M and Tokumitsu E 2005 *Appl. Phys. Lett.* **86** 162902
[7] Nayak P K, Hedhili M N, Cha D and Alshareef H N 2013 *Appl. Phys. Lett.* **103** 033518
[8] Koida T, Fujiwara H and Kondo M 2008 *J. Non-Cryst. Solids* **354** 2805
[9] Kobayashi E, Watabe Y and Yamamoto T 2015 *Appl. Phys. Express* **8** 015505
[10] Koida T, Ueno Y and Shibata H 2018 *Phys. Status Solidi* a **215** 1700506
[11] Meng F, Shi J, Liu Z, Cui Y, Lu Z and Feng Z 2014 *Sol. Energy Mater. Sol. Cells* **122** 70
[12] Newhouse P F, Park C-H, Keszler D A, Tate J and Nyholm P S 2005 *Appl. Phys. Lett.* **87** 112108
[13] Gupta R K, Ghosh K, Mishra S R and Kahol P K 2008 *Appl. Surf. Sci.* **254** 1661
[14] Lu Z, Meng F, Cui Y, Shi J, Feng Z and Liu Z 2013 *J. Appl. Phys.* **46** 075103
[15] Shigesato Y, Koshi-ishi R, Kawashima T and Ohsako J 2000 *Vacuum* **59** 614
[16] Sun X W, Huang H C and Kwok H S 1996 *Appl. Phys. Lett.* **68** 2663
[17] Furubayashi Y, Maehara M and Yamamoto T 2019 *Nanoscale Res. Lett.* **14** 120
[18] Yamamoto T, Song H and Makino H 2013 *Phys. Status Solidi* C **10** 603
[19] Shirakata S, Sakemi T, Awai K and Yamamoto T 2006 *Superlattices Microstruct.* **39** 218
[20] Suzuki Y, Niino F and Katoh K 1997 *J. Non-Cryst. Solids* **218** 30
[21] Harrison W A 1989 *Electronic Structure and the Properties of Solids: The Physics of the Chemical Bond* (Mineola, NY: Dover Publications)
[22] Mann J B 1968 *Atomic Structure Calculations II. Hartree-Fock Wave Functions and Radial Expectation Values: Hydrogen to Lawrencium* (Los Alamos, NM: Los Alamos Scientific Laboratory)

[23] Luo Y R 2007 *Comprehensive Handbook of Chemical Bond Energies* (Boca Raton, FL: CRC Press)
[24] Koida T 2017 *Phys. Stat. Solidi* a **214** 1600464
[25] Patterson A L 1939 *Phys. Rev.* **56** 978
[26] Zeng L *et al* 2018 *Phys. Rev. Mater.* **2** 053401
[27] Kröger F A and Vink H J 1956 *Solid State Phys.* **3** 307
[28] Ioffe A F and Regel A R 1960 *Prog. Semicond.* **4** 237
[29] Zeng F, Zhang X, Wang J, Wang L and Zhang L 2004 *Nanotechnology* **15** 596
[30] Liang C, Meng G, Lei Y, Phillip F and Zhang L 2001 *Adv. Mater.* **13** 1330
[31] Thomson J J 1901 *Proc. Cambridge Philos. Soc.* **11** 120